Disruption of microbial communication yields a two-dimensional percolation transition

Kalinga Pavan T. Silva, Tahir I. Yusufaly, Prithiviraj Chellamuthu, and James Q. Boedicker

Phys. Rev. E **99**, 042409 — Published 19 April 2019

DOI: 10.1103/PhysRevE.99.042409

Disruption of microbial communication yields a 2D percolation transition

Kalinga Pavan T. Silva[1], Tahir I. Yusufaly[1], Prithiviraj Chellamuthu[1], James Q. Boedicker[1,2]
[1]University of Southern California, Department of Physics and Astronomy
[2]University of Southern California, Department of Biological Sciences

Bacteria communicate with each other to coordinate macro-scale behaviors including pathogenesis, biofilm formation and antibiotic production. Empirical evidence suggests that bacteria are capable of communicating at length scales far exceeding the size of individual cells. Several mechanisms of signal interference have been observed in nature, and how interference influences macro-scale activity within microbial populations is unclear. Here we examined the exchange of quorum sensing signals to coordinate microbial activity over long distances in the presence of a variable amount of interference through a neighboring signal-degrading strain. As the level of interference increased, communication over large distances was disrupted and at a critical amount of interference, large-scale communication was suppressed. We explored this transition in experiments and reaction-diffusion models, and confirmed that this transition is a 2D percolation transition. These results demonstrate the utility of applying physical models to emergence in complex biological networks to probe robustness and universal quantitative features.

I. INTRODUCTION

Recent years have seen increasingly clear evidence that the traditional view of bacteria as `loner' organisms must be revised [1–5]. In natural habitats, diverse microbial species regularly interact with each other and their environment, and such interactions frequently have a profound effect on the resulting microbial phenotypes [6–8]. For example, a commonly found interaction is signal interference, and one commonly found interference mechanism is where signals produced by one type of species are degraded by a different species, which in turn will affect cellular activity and gene expression [1].

From a physics perspective, such multispecies communities offer a novel context in which to discover and characterize emergent, collective phenomena in strongly interacting many-body networks [9–13]. One particularly notable and relevant example of such collective behavior is percolation, where networks display an abrupt transition in large-scale global connectivity at a critical threshold of a varying parameter, typically occupation probability. Percolation is an attractive topic to physicists for several reasons, the most important one arguably being its universality – the fact that systems which are quite dissimilar microscopically display equivalent quantitative scaling behavior near the transition [14–16]. While percolation has been observed and analyzed in numerous abiotic contexts, other than a recent report [13] there is relatively little work exploring its implications for biological systems, particularly community-level ecosystems. It remains a challenge to identify suitable 'model' community-level networks in which to explore potential biological realizations of percolation. An ideal system should be simultaneously experimentally and theoretically tractable, while also being capable of yielding qualitative and quantitative insight into the workings of real microbial communities *in situ*. Microbial communication networks are a particularly strong candidate for such a system.

Bacteria use small chemical signals known as autoinducers (AI) to communicate with their neighbors. The basic process of communication, known as quorum sensing [2,17–20], involves cells secreting, sensing, and responding to a threshold concentration of AI molecules, thereby regulating density-dependent gene expression. Quorum sensing (QS) regulates several collective, group-level behaviors, including pathogenesis [21,22], biofilm formation [23], antibiotic production [1,24,25], and bioluminescence [20]. Empirical evidence suggests that these behaviors can span large distances [9,20,26] .

In this work, we examine the robustness of such communication networks to interference by analyzing spatial patterns of activation in a model bacterial community consisting of a sender cell, which produces and responds to AI signals, and a degrader cell, which produces an enzyme capable of destroying the signal, as shown in Fig. 1(a) and similar to strains used in previous studies [27,28]. This model community allows a controlled, systematic study of interactions that occur naturally within microbial ecosystems [29,30]. For example, *Bacillus subtilis*, a Gram-positive bacteria commonly found in soil, secretes the degradative enzyme AiiA used in the study. In its natural environment, *B. subtilis* interacts with many soil strains that use AHL-based quorum sensing, including species of *Pseudomonas*, *Serratia*, and *Eneterobacter* [31]. We explore through both experiments and theoretical models how the ratio of these two strains influences the ability of the senders to communicate over long distances. Our primary result is the discovery of a percolation transition that leads to a sudden breakdown in long-range communication at a critical strain ratio. We observe universal critical scaling exponents at the transition that are independent of the specific properties of individual strains, and show that the specific transition point can be shifted in a predictable way by selective genetic modification of strains.

II. EXPERIMENTS ON QUORUM SENSING BACTERIA

A. Experimental setup

An experimental assay was developed to test the capability of microbes to coordinate activity in spatially structured environments. As shown in Fig. 1(b), a specified ratio of sender and degrader cells were mixed together and applied to the top of an LB agar plate. Cells emit diffusible signals and spread out via cell division, but are not motile. Sender cells are a strain of *Escherichia coli* containing the LuxRI quorum sensing system and a GFP reporter gene for quorum sensing activation. Senders increase the expression of the GFP reporter gene in response to an increase in the concentration of a diffusible signaling molecule, here acyl-homoserine lactones (AHL). The response function of GFP production is non-linear, exhibiting a sharp increase in cellular fluorescence when the amount of signal exceeds a threshold concentration [26,32]. Degrader cells are a strain of *E. coli* constitutively expressing the lactonase enzyme AiiA [27]. AiiA remains inside the degrader cells and degrades AHL quorum sensing signals that diffuse into the cell, including the 3-oxo-C6-HSL produced by the sender cells [26,33].

B. Experimental results

In the presence of degraders, both the degrader and sender cells influence the local concentration of signal. In regions where, by chance, degrader cells are more abundant, AHLs will be depleted and potentially dip below the threshold concentration needed for activation. Consequently, senders will not activate GFP expression and will appear dark in fluorescent images. In Fig. 2(a), we have a sender strain, distributed with the degrader strain, at a ratio of 10^9:6 x 10^8 (sender: degrader). Here, we observe that in the regions where degraders are more abundant, senders have not activated GFP (see also Fig. S1 [34]). To determine whether a sender has activated quorum sensing or not, we define a fluorescence intensity threshold for activation, which was 25% of the maximum detected GFP value (see Fig. S2 [34]). The validity of the threshold we chose and the robustness of our results to slight changes in threshold will be discussed later. The activation of quorum sensing in the sender cells was monitored using fluorescence microscopy. The sender cells that activate quorum sensing express high levels of GFP and appear green in the fluorescent microscopy images shown in Fig. 2(a), Fig. 2(b), whereas sender cells that did not activate quorum sensing are dark and not visible. Plates are imaged at 20x magnification 16 hours after inoculation. For each image the field of view spans an area of 750 µm x 630 µm, and a minimum of 16 fields of view were imaged for each experimental condition.

As shown in Fig. 2(b), when no degrader cells are added to the plate, all the senders activate quorum sensing and produce green fluorescence throughout the plate. On plates containing a mixture of degrader and sender cells, dark regions were observed that represent regions where the quorum sensing signal did not accumulate above the threshold concentration required for activation. The sizes of these inactivated regions were larger in plates containing more degrader cells, and activation was completely inhibited when more than 10^9 cells of degrader were spread onto the plate. As seen in Fig. S3 [34], introducing a dummy strain that is the same strain of *E. coli*, but which does not contain the

plasmid necessary for producing the signal degrading enzyme, did not result in dark patches in the fluorescence image, even when the dummy strain was loaded 3 times higher than the sender strain. This demonstrates that inhibition of quorum sensing activity is due to the depletion of the signal concentration, and not caused by competition between the two strains for resources or space. This is further validated with Fig. S4 [34], where we introduce the sender strain, which produces RFP constitutively, and observe that even for high amounts of degrader, the senders seem to occupy most of the plate. For all experiments, we load 10^9 senders, as it gives a near uniform distribution of the cells on the plate (see Fig. S5 [34]).

The transition from large connected regions of activation to segregated patches of activation observed in Fig. 2(b) appears similar to a percolation transition. In percolating systems, regions of activity have a sharp transition in connectivity above a critical value of control parameters [35,36]. Here the control parameter is the amount of degrader cells in the population. The connectivity of activated regions is quantified by measuring percolation events. A percolation event occurs when at least one continuous region of activation spans the entire system. In our experiments, percolation is defined as a continuous region of fluorescence intensity above a threshold value that touches opposite sides of the image, a region of space 750 µm x 630 µm. As discussed above, this threshold (thr) was selected to be 25% of the maximum fluorescent intensity detected by the microscope (thr = 148) (see Fig. S2 [34]). By applying this threshold, we obtain the amount of pixels above this threshold, and we observe that the amount of active pixels are largely robust when the threshold is changed by up to 20% from the value we select (see Fig. S6 [34]).

We quantified percolation in each fluorescent image. Fig. 2(c) shows the percentage of images that exhibited percolation (percolation frequency) for each amount of degrader cells tested. At low numbers of degraders, there will always be a percolation event. Once the density of degraders reaches a critical value near $3x10^8$ cells, the percolation frequency rapidly decreases towards zero.

Percolation has been observed in many diverse physical systems, including dielectric breakdown [37], porous transport [38], and even the epidemiology of infectious diseases [39]. The properties of such percolation networks are known to follow characteristic scaling laws. We measured values for critical exponents associated with the scaling laws for three well known quantities from 2D-percolation theory [16,40]: the average cluster size <s>, the order parameter P_∞ and the correlation length ξ. For this analysis, pixels in the fluorescent images are assigned a value of active or "occupied" if the fluorescent intensity is above the threshold (thr), or conversely a value of inactive or "empty" if the fluorescent intensity is below threshold. If an active pixel is touching another active pixel in either of the 8 neighboring positions, we define these two pixels as being connected. If a connection of pixels spreads from one edge of the image to its opposite edge, we define this collection of active pixels as a spanning cluster.

To obtain the average cluster size <s>, we measured the areas of all the clusters of activated pixels, excluding pixels in the spanning cluster, and took the average of the measurements. The order parameter, $P_{\infty,}$ is defined as the probability that an activated pixel belongs to the spanning cluster, and was determined by taking the ratio of the number of active pixels in the spanning cluster to the total number of active pixels in all clusters. Finally, the correlation length ξ measures the length scale over which activation is correlated; in other words, if a given pixel is activated, it is expected that, on average, pixels within a distance ξ of that pixel would also be activated. To obtain ξ, we considered the largest non-spanning cluster, and calculated the average distance between two pixels within this cluster. These three quantities are plotted in Fig. 3. In the classical theory these quantities are generally plotted against the occupation probability [40]. In Supplementary Material section VII, Table S1 and Fig. S7 [34], we show that at the transition, the occupation probability scales essentially linearly with the amount of degraders. As a result of this linear relationship, all quantities are expected to have the same universal scaling behavior with respect to the amount of degraders: $\langle s \rangle \propto |n_{AiiA} - n_{AiiA\ c}|^{-\gamma}$, $P_\infty \propto |n_{AiiA} - n_{AiiA\ c}|^{\beta}$, $\xi \propto |n_{AiiA} - n_{AiiA\ c}|^{-\nu}$, where, n_{AiiA} is the amount of degraders, $n_{AiiA\ c}$ is the critical amount of degraders at the percolation threshold, and γ, β and ν are the critical exponents for the transitions of average cluster size, order parameter and correlation length respectively. We determined $n_{AiiA\ c}$ to be 6.5×10^8 by considering the n_{AiiA} at which we observe maximal values of the

average cluster size and correlation length [40] (see Fig. S8 [34]).

We find that the experimentally measured exponents are consistent with the expected values for a standard 2D percolation transition [16,40], as shown in Fig. 3 and Table 1. To calculate the critical exponents, we generated a $\log_{10}$-$\log_{10}$ transform of the scaling quantities near the critical point, see Fig. S9, [34] and calculated the gradient of a linear fit via least squares regression, with uncertainties determined via the standard error of the slope, as shown in in Table 1. In Supplementary material [34], we further justify these results via additional tests of the robustness of the critical exponents to changing thresholds. The calculated critical exponents were not sensitive to the exact number of points fit nor the 20% changes in the threshold value used to classify activated pixels, (see Fig. S10 and S11 [34]). Such scaling rules should be independent of the scale over which they are observed, and to demonstrate this scale-free nature of our results, we reanalyzed the data for a different sized imaging window and found the calculated exponents were similar (see Fig. S12, Supplementary Table S2 [34]).

III. MATHEMATICAL MODEL

A. Reaction-diffusion model

To obtain a deeper understanding of the transition, we can compare these experimental results to numerical simulations of the underlying biochemical kinetics. We developed a model that captured the dynamics of signal exchange and cell growth. The growth of the cells is modeled with a logistic growth equation [9,26],

$$\frac{\partial n_i}{\partial t} = \mu\, n_i\left(1-\frac{n_t}{s}\right). \qquad (1)$$

Here, *i* can be either AHL or AiiA, where n_{AHL} represents the number of sender cells and n_{AiiA} represents the number of degrader cells such that the senders and degraders will have separate logistic growth equations. The total cell number (n_t) is equal to the number of sender cells plus the number of degrader cells at a particular location in space. Each cell grows exponentially with rate μ such that n_t approaches a saturated cell number (s), at which point growth will cease ($n_t \leq s$). The dynamics of the signals produced by the senders and the degradative enzymes produced by the degraders can be described by reaction diffusion equations,

$$\frac{\partial [AHL]}{\partial t} = D_{AHL}\nabla^2[AHL] - \gamma_1[AHL] + n_{AHL}\left(\rho_{AHL}\frac{[AHL]^{m_1}}{[AHL]^{m_1}+{\theta_1}^{m_1}} + \rho_{b1}\right) - \gamma_2[AiiA]\frac{[AHL]^{m_2}}{[AHL]^{m_2}+{\theta_2}^{m_2}}\,. \qquad (2)$$

The AHLs are initially produced at a lower basal rate of ρ_{b1}, by n_{AHL} number of sender cells, (n_{AHL} governed by Equation (1)), and the AHL concentration ([AHL]) increases over time. AHLs will diffuse into the media with a diffusion coefficient of D_{AHL}. Once the concentration builds up to a critical threshold value of θ_1, the production rate of AHLs increases by ρ_{AHL}. This switching from the lower to higher production rate is represented by a Hill function with a Hill coefficient of m_1. The AHLs are degraded in the media at a rate of γ_1, and by the degradative enzyme at a rate γ_2. The degrader enzyme concentration is [AiiA] and the amount of signals degraded is regulated by the presence of the signal. We represent this by an additional Hill function with a Hill coefficient of m_2, where the AHL concentration needs to accumulate beyond a critical number to get a considerable amount of degradation [26,27]. Note that, unlike the AHLs, the degrader enzymes do not freely diffuse throughout the medium, but are localized within the degrader cells. The degraders will constitutively produce the degradative enzyme at a rate of ρ_{AiiA} within the degrader cells, a protein which decays at a rate of γ_3.

$$\frac{\partial [AiiA]}{\partial t} = n_{AiiA}\rho_{AiiA} - \gamma_3[AiiA]\,. \qquad (3)$$

Here, the number of degrader cells, n_{AiiA}, is governed by equation (1). In simulations, sender and degrader cells are initially distributed randomly within an area of 0.49 mm^2. In this area there are 22500 pixels (150 x 150) and each pixel has a size of approximately 25 μm^2. Each pixel can hold approximately 25 cells. Sender cells are fixed and distributed homogenously while the degraders will change and be distributed randomly. Cells do not move over time, but spread to adjacent regions of the plate due to cell growth. Signal is produced and degraded over time, reaching a steady-state AHL

concentration profile within 16 hours. Regions of space where the signal concentration is above the quorum sensing threshold (θ_1) are plotted, as shown in Fig. 4(a). These would correspond to regions of high fluorescent intensity in experiments. All the values for the parameters are taken from Silva et al. [26], and reported in supplementary Table S1.

B. Modelling results

As in experiments, we first obtain the percolation frequency as a function of the amount of degraders, and, as shown in Fig. 4(b), observe that at 10^8 cells the percolation frequency decreases, similar to experimental observations. Subsequently, the same image processing algorithms that we apply to calculate <s>, P_∞ and ξ from experimental activation maps are applied to simulation outputs, allowing us to plot <s>, P_∞ and ξ from simulations and calculate the critical exponents, as shown in Fig. 4(c), Table 1 and Fig. S13 [34]. Via finite-size-scaling analysis, similar to the windowing we perform on experimental images, we observe that as system size increases, the exponents systematically converge onto the expected classical value for an infinite system (see Fig. S14, S15 and Table S3 [34]).

As shown in Fig. S14b [34], finite size effects likely contribute to lowering values of P_∞ near the percolation transition. The fluorescence threshold value (thr) also artificially lower the values of P_∞ through its influence on the size of clusters, including the spanning cluster. As shown in Fig. S16 [34], reducing the threshold shifts values of P_∞ upward towards the simulated values. However, as seen in Fig. S2 and Fig. S6 [34], the reduced threshold is near the fluorescence background and results in difficulty in identifying activated regions from background noise. Although at the threshold value used the experimental and simulated measurements of P_∞ are not identical, this did not change the qualitative behavior or the values of the critical exponents calculated from experiments.

The behavior of the scaling quantities near criticality and the values obtained from experiments and theory revealed that when a signal degrading strain is added to a spatial cellular network, the breakdown of effective communication follows a sharp transition whose spatial distribution of activity follows a percolation transition. The senders' capability to coordinate activity over large distances via the exchange of quorum sensing signals fails if the amount of degrader cells exceeds approximately $3x10^8$ cells. The critical amount of degrader cells leading to this transition is a tunable parameter.

IV. SHIFTING THE TRANSITION POINT BY CHANGING THE PRODUCTION RATE OF AIIA

In simulations, we observe that changing the production rate of degradation enzyme per cell shifted the critical number of degraders required to disrupt long distance communication, as shown in Fig. 5(a). To validate this observation experimentally, we constructed a new degrader strain with tunable expression of the *aiiA* gene (see Fig. S17a and b [34]). By introducing isopropyl β-D-1-thiogalactopyranoside (IPTG) at different concentrations, the expression level of *aiiA* is controlled. When the senders are mixed with the new degrader strain in a plate reader, we observe that the steady state fluorescence decreases with increasing IPTG, confirming that production of the degradative enzyme is regulated by the inducer (see Fig. S17c [34]).

TABLE 1. Values of the critical exponents**.** The values here represent the slope of the $\log_{10}$-$\log_{10}$ linear fit. The linear fits were performed using least square fitting method, and the uncertainty here is the standard error (SE) of the slope represented as SE$= \frac{\sqrt{\sum \frac{(yi-\hat{y}i)^2}{(n-2)}}}{\sqrt{\sum (xi-\bar{x})^2}}$, where, yi is the dependent variable value for point *i*, $\hat{y}i$ is the dependent variable value for point *i* from the least square fit, xi is the independent variable value for point *i*, $\bar{x}$ is the mean of the independent variable, and n is the number of observations.

Critical exponents	For the average cluster size (γ)	For the order parameter (β)	For the correlation length (ν)
2D percolation universality class	2.39	0.14	1.33

From experiments	2.28 ± 0.36	0.17± 0.06	1.36± 0.12
From reaction-diffusion simulations	2.42± 0.16	0.16± 0.03	1.35 ± 0.06

In Fig. 5(b), similar to the simulation results, we observe that the critical degrader amount can be shifted in experiments by increasing the production rate of the degradative enzyme by introducing 1 mM of IPTG to the plate. We calculated the critical exponents for the case of increased AiiA production and once again obtain similar values to the classical theory (see Supplementary Table S4). In Fig. 5, we also have shown the universality in the nature of the transition by changing the coordinates in the $\log_{10}$ (Amount of degraders) axis by reducing it to ($\log_{10}$ (Amount of degraders) - $\log_{10}$(Amount of degraders)$_c$)/ ($\log_{10}$(Amount of degraders)$_c$), where $\log_{10}$(Amount of degraders)$_c$ is the point at which the percolation frequency goes to zero.

V. DISCUSSION

With the recent advances in systems and molecular biology, many new studies are being conducted to understand the complex behaviors of microbes that arise due to cellular and spatial heterogeneity [9,26–28,41–44]. Several studies have shown that many cellular systems exhibit emergent phenomena previously studied in non-biological contexts and that can be explained using physical and statistical mechanical rules [45–48]. For instance, Wioland et al. discuss the capability of bacterial vortices, whose lattices are hydrodynamically coupled, to spontaneously form into distinct patterns characterized by ferro- and antiferromagnets [45]. Rudge et al. observed the emergence of striking fractal patterns in growing colonies of *E. coli* [48]. Physical models such as the Hopfield model have also been implemented to predict how the capacity for groups of cells to make decisions scales with the number of cell types [44]. In the spirit of these observations, here we have identified that disrupting the long-range communication of a quorum sensing microbe through interference by a degrader strain yields complex physical behavior characteristic of a percolation transition. Critical transitions in cellular distributions have been previously reported. For example, Ratzke et al. reported that agar concentration tuned the distribution of cells from one large cluster to small patchy clusters [49]. However, this phenomena was not analyzed as a percolation transition. More recently, a percolation transition was reported for electrochemical signaling in biofilm of *Bacillus subtilis* [13] . As was observed in the quorum sensing network, the connectivity of active cells sharply changed at a critical point and the cluster size of active cells scaled as a power law. These studies emphasize the utility in applying physical models to study biological networks and their emergent behaviors, an approach that is expected to continue to yield insights into the fundamental capabilities of these systems and potentially reveal new strategies for robust control of system function.

In our specific systems, it was particularly surprising that the spatial distribution of quorum sensing activity was extremely sensitive to the number of degrader cells. Although in well mixed simulations (see Fig. S18 [34]), we observed a similar ratio of degraders to senders of 1:2 was needed to turn off the senders. The long distance coordination of quorum sensing activity was robust to small amounts of interference by degraders, but as the number of degrader cells approached the number of sender cells there was a sharp change in the connectivity of activated regions. The cellular network transitioned from large connected regions of activity to smaller patches of active cells over a factor of 10 change in cell number, and this change followed a classic 2D percolation transition. These results demonstrate that cellular networks can undergo critical changes in behavior as a function of the ratio of cell types.

In our previous work [26], we analyzed how signal degrading cells influence the spatial range over which a colony of sender cells can activate a circular pattern of quorum sensing up to a maximum radius that depended on the number of degrader cells. Here, we examined spatial patterns of activation that naturally emerge from well mixed populations of sender and degrader strains, and revealed scale-free patterns of quorum sensing activation that fit the definition of a percolation transition.

Since changes in signaling states, including quorum sensing activation, are important for many coordinated functions of cellular networks, including virulence and biofilm formation [17,50], small changes in the composition of a community might be a strategy to control the global function of microbial communities. Successful implementation of such a strategy requires knowledge of the critical point of the transition and how it scales with system parameters, such as enzyme activity, protein expression, and growth dynamics. In our system, additional theoretical analysis in the Supplementary Text 1 determined the major factors that dictate the transition point of percolation were the degradation rate of the AHLs by the AiiA enzyme, the degradation of the AiiA enzyme by the media, the production rate of the AHLs and the production rate of the AiiA enzyme. Here we demonstrated that the critical point can indeed be tuned by changing the production rate of the signal degrading enzyme.

When analyzing our results as a 2D percolation transition, the critical exponents were calculated in both experiments and theoretical simulations [16,40]. The slight changes in the exponent values from the experiments compared with the classical theory can be attributed to the inefficiencies in measurements caused by subtle inhomogeneity in the cell distributions, and to the fact that we are using a finite system as opposed to an infinite system [14,15]. Through additional image analysis such as windowing and finite scaling, we observed that the values of the critical exponents are robust universal quantities, with fairly small deviation from the infinite classical values even as the system size gets smaller.

Future work in this direction should investigate signaling dynamics within more complex environments, such as those found *in situ*, to see if there are instances where the qualitative network behavior can indeed be described by ordinary percolation. Since quorum sensing enables bacteria to exchange information regarding the local environment [1,18,20], the consequences of breaking down such communication by interference raises questions about how cells have evolved to coordinate activity in the presence of interference. The patterns that emerged in our experiments were stable for many hours, although how the activity of cellular networks evolves over much longer time periods and the consequences of being far-from-equilibrium warrant further study. The critical behavior observed here is yet another example of biological systems operating near critical conditions [46,47,51–57]. Examination of natural signaling networks that have been tuned to function in the vicinity of a percolation transition should help to understand the importance of criticality in such biological contexts.

VI. METHODS

A. Bacterial strains

The sender strain is *Escherichia coli* (NEB 5-alpha) with the plasmid pTD103luxI sfGFP(Kn) obtained from Prindle et al. [28] Here, *luxI, luxR* and *sfGFP* are under the *luxIP* quorum sensing promoter. When quorum sensing has been activated, the senders will turn on a green fluorescent response.

The degrader strain is *Escherichia coli* (NEB 5-alpha) with the plasmid pTD103aiiA_lac (see Fig. S17a [34]). This plasmid was constructed by mutagenesis, using NEB Q5® site-directed mutagenesis kit, by replacing the *luxIp* promoter in the plasmid pTD103aiiA obtained from Prindle et al. [28] with the *lacUV5* constitutive promoter. The degradative enzyme, AiiA, is constitutively produced under *lacUV5* promoter.

The strain with the lower AiiA production rate was constructed by Gibson assembly, using the NEB Gibson assembly® master mix, by replacing the *yfp* gene sequence in the plasmid pZS25O1+11-YFP, obtained from Garcia et al. [58], with the *aiiA* gene sequence (see Fig. S17b [34]). The *aiiA* gene sequence was obtained from pTD103aiiA_lac. Since the new plasmid pZS25O1+11_AiiA has the O1 repressor binding site, the expression level of the AiiA enzyme can be controlled by isopropyl β-D-1-thiogalactopyranoside (IPTG). Primers used for the mutagenesis and Gibson assembly are given in Table 2. The constitutive red fluorescent sender strain was constructed by electroporation of the plasmid pTD103luxI sfGFP(Spec) into the *Escherichia coli* TK140 pZS25O1+11-mCherry obtained from Garcia et al. [58].For the dummy strain in Fig. S3 [34] we used the strain, *Escherichia coli* TK140 pZS25O1+11-mCherry obtained from Garcia et al. [58].

TABLE 2. Primer sequences used for making the plasmids.

Name	Function	Sequence
AiiA LacUV5 F	The forward primer to replace the luxIP promoter from pTD103aiiA with the lacUV5 vector to construct the plasmid pTD103aiiA_lac.	GGCTCGTATAATGTGTGGGAATTCATTAAAGAGGAGAA AG
AiiA LacUV5 R	The reverse primer of the above.	GGAAGCATAAAGTGTAAAGCTTATGTTAAGTAATTGTAT TC
pZS_YFP_1F	The forward primer used to obtain the plasmid backbone, excluding the YFP, from the plasmid pZS25O1+11-YFP for the construction of the plasmid pZS25O1+11_AiiA.	GAA AAT TAC GCC CTT GCA GCG TAA AAG CTT AAT TAG CTG A
pZS_YFP_1R	The reverse primer of the above.	CTG GGA TGA AAT AAA GTT TCT TTA CTG TCA TTG CGG TAC CTT TCT C
pZE_AiiA_F	The forward primer used to obtain the vector *aiiA* from the plasmid pTD103aiiA_lac for the construction of pZS25O1+11_AiiA.	GGA GAA AGG TAC CGC AAT GAC AGT AAA GAA ACT TTA TTT CAT CCC AG
pZE_AiiA_R	The reverse primer of the above.	GAC TCA GCT AAT TAA GCT TTT ACG CTG CAA GGG CGT AAT TTT C

B. Bacterial growth conditions

Similar to Silva et al. [9], the cells were grown in 5ml of Lysogenic broth (LB) which were in 14mL Falcon tubes with appropriate antibiotics for plasmid maintenance. The cultures were put into a shaker at 200 RPM and 37 ^{o}C. Cells were grown in liquid culture for 16 hours.

C. Bacterial strains

In experiments, sender culture was transferred to a micro centrifuge tube and centrifuged it at 15000 RPM for 1min. The supernatant was discarded, cells were re-suspended in fresh media, cell number was adjusted to 10^9 sender cells, and a variable amount of degrader cells were added. The final volume of culture was 1 mL, such that the volume of culture loaded onto the LB-agar plate was the same in all experiments. The 1 mL mixture with 10^9 : n amount of sender: degrader, was pipetted on to a 3 mm LB-agar Petri dish (see Fig. 1(b)). This plate was then incubated at 37 ^{o}C for 16 hours.

D. Microscopic measurements and image analysis

After 16 hours growth the plate was loaded into a Nikon eclipse TI fluorescent microscope and GFP fluorescent images were obtained at a magnification of 20x. Exposure time was 500 ms. The images were analyzed in Matlab 2016b using custom analysis algorithms. For each plate, a minimum of 16 different regions were imaged and analyzed.

In these codes, we first set the same threshold value (thr) for fluorescence intensity to identify quorum sensing activated regions. Each pixel had an intensity value of 1 or 0 representing quorum sensing activation or non-activation respectively. Next, each activated cluster is identified and assigned a number. If an activated pixel is being occupied by a neighboring pixel (including diagonal neighbors), the two pixels are considered to be in the same activated cluster. After the activated clusters are labeled, we looked at whether active clusters spanned from top to bottom or left to right to determine if for each image, a percolation transition occurred. Next properties such as, areas of clusters and mean distance between two active pixels within the same cluster was determined to obtain the scaling properties mentioned in the manuscript.

VII. ACKNOWLEDGEMENTS

We thank Stephan Haas for helpful discussions. This work was supported by Office of Naval Research award number N00014-15-1-2573 and NSF PHY-1753268. JB was supported by DARPA YFA Grant No. D16AP00121.

References

[1] G. Rampioni, L. Leoni, and P. Williams, Bioorg. Chem. **55**, 60 (2014).
[2] J. Boedicker and K. Nealson, IEEE Trans. Mol. Biol. Multi-Scale Commun. **1**, 310 (2016).
[3] S. P. Darch, S.E., West, S.A., Winzer, K. , Diggle, Proc. Natl. Acad. Sci. **109**, 8259 (2012).
[4] M. B. Miller and B. L. Bassler, Annu. Rev. Microbiol. **55**, 165 (2001).
[5] J. Friedman and J. Gore, Curr. Opin. Syst. Biol. **1**, 114 (2017).
[6] B. Kirkup, U. States, M. Woods, and H. Oceanographic, Science (80-.). **337**, (2012).
[7] M. Marı, N. Fuster-valls, M. Herna, and J. Rodrı, Food Control **19**, 308 (2008).
[8] F. Wu, D. J. Menn, and X. Wang, Chem. Biol. **21**, 1629 (2014).
[9] K. P. T. Silva, P. Chellamuthu, and J. Q. Boedicker, PLoS Comput. Biol. **13**, 1 (2017).
[10] T. I. Yusufaly and J. Q. Boedicker, Phys. Rev. E **94**, 62410 (2016).
[11] M. R. Frederick, C. Kuttler, B. A. Hense, J. Müller, and H. J. Eberl, Can. Appl. Math. Q. **18**, 267 (2011).
[12] Y. B. Tatek and G. W. Slater, Physica A **362**, 2 (2006).
[13] J. W. Larkin, X. Zhai, K. Kikuchi, S. E. Redford, A. Prindle, J. Liu, S. Greenfield, A. M. Walczak, J. Garcia-Ojalvo, A. Mugler, and G. M. Süel, Cell Syst. **7**, 137 (2018).
[14] R. Kenna and B. Berche, J. Phys. A **50**, 1 (2017).
[15] Y. Zhu and X. Chen, Cond-Mat.Stat-Mech **818**, 1 (2017).
[16] L. L.-S. YU Mei-Ling, XU Ming-Mei, LIU Zheng-You, Chinese Phys. C **33(7)**, 552 (2009).
[17] S. T. Rutherford and B. L. Bassler, Cold Spring Harb Perspect Med **2**, 1 (2012).
[18] P. Williams, K. Winzer, W. C. Chan, and M. Cámara, Philos. Trans. R. Soc. London B Biol. Sci. **362**, 1119 (2007).
[19] K. H. Mcclean, M. K. Winson, L. Fish, A. Taylor, S. R. Chhabra, M. Camara, M. Daykin, H. John, S. Swift, B. W. Bycroft, G. S. A. B. Stewart, and P. Williams, Microbiology **143**, 3703 (1997).
[20] K. H. Nealson and J. W. Hastings, Appl. Environ. Microbiol. **72**, 2295 (2006).
[21] R. Teresa and B. H. Iglewski, Infect. Immun. **68**, 4839 (2000).
[22] B. Lasarre and M. J. Federle, Microbiol. Mol. Biol. Rev. **77**, 73 (2013).
[23] J. S. Dickschat, Nat. Prod. Rep. **27**, 343 (2010).
[24] A. M. L. Barnard, S. D. Bowden, T. Burr, S. J. Coulthurst, R. E. Monson, and G. P. C. Salmond, Philos. Trans. R. Soc. London B Biol. Sci. **362**, 1165 (2007).
[25] K. Anguige, J. R. King, and J. P. Ward, J. Math. Biol. **51**, 557 (2005).
[26] K. P. Silva, P. Chellamuthu, and J. Q. Boedicker, Biophys. J. **112**, 1037 (2017).
[27] L. Tsimring, J. Hasty, T. Danino, O. Mondrago, O. Mondragón-Palomino, L. Tsimring, and J. Hasty, Nature **463**, 326 (2010).
[28] A. Prindle, P. Samayoa, I. Razinkov, T. Danino, L. S. Tsimring, and J. Hasty, Nature **481**, 39 (2012).
[29] Y. Dong, J. Xu, X. Li, and L. Zhang, Proc. Natl. Acad. Sci. **97**, 3526 (2000).
[30] C. Grandclement, T. Melanie., S. Mor, Y. Dessaux, and D. D. Faure, FEMS Microbiol. Rev. **40**, 1 (2015).
[31] C. Tmin and C. Koh, Sensors **12**, 4846 (2012).
[32] A. Pai, Y. Tanouchi, and L. You, Proc. Natl. Acad. Sci. **109**, 19810 (2012).

[33] F. Constantinescu, L. Michel, and C. Reimmann, FEMS Microbiol. Ecol. **45**, 71 (2003).
[34] See Suplemental Material at for further information on fluorescent images representing the uniform spreading of the senders, robustness analysis of the threshold chosen, theoritical derivation of the linear behaviour near the critical point, simulation results for extracting the critical exponents, windowing anaysis of the experiments, finite scaling analysis of the simulations and further details on the strans used in this study.
[35] R. M. Ziff, Phys. Rev. Lett. **69**, 2670 (1992).
[36] S. N. Dorogovtsev, A. V Goltsev, and J. F. F. Mendes, Rev. Mod. Phys. **80**, 1 (2008).
[37] J. H. Stathis, J. Appl. Phys. **86**, 5757 (1999).
[38] K. L. and J. F. W. Richard Chandler, Joel Koplik, J. Fluid Mech. **119**, 249 (1982).
[39] R. Parshani, S. Carmi, and S. Havlin, Phys. Rev. Lett. **258701**, 1 (2010).
[40] A.-L. Barabási, G. Musella, N. Samay, R. Sinatra, S. Morrison, A. Husseini, and P. Hoevel, CC BY-NC-SA 2.0 (2014).
[41] E. Ben-jacob, M. Lu, D. Schultz, and J. N. Onuchic, Front. Cell. Infect. Microbiol. **4**, 1 (2014).
[42] P. Freemont, K. M. Polizzi, and L. Goers, J. R. Soc. Interface **11**, 1 (2014).
[43] J. C. March and W. E. Bentley, Curr. Opin. Biotechnol. **15**, 495 (2004).
[44] T. I. Yusufaly and J. Q. Boedicker, Phys. Biol. **14**, 1 (2017).
[45] H. Wioland, F. G. Woodhouse, J. Dunkel, and R. E. Goldstein, Nat. Phys. **12**, 341 (2016).
[46] J. Hidalgo, J. Grilli, S. Suweis, M. A. Muñoz, J. R. Banavar, and A. Maritan, Proc. Natl. Acad. Sci. **111**, 10095 (2014).
[47] X. Chen, X. Dong, A. Be, H. L. Swinney, and H. P. Zhang, Phys. Rev. Lett. **148101**, 1 (2012).
[48] T. J. Rudge, P. J. Steiner, A. Kan, and J. Haselo, ACS Synth. Biol. **2**, 705 (2013).
[49] C. Ratzke and J. Gore, Nat. Microbiol. **1**, 1 (2016).
[50] J. D. Shrout, D. L. Chopp, C. L. Just, M. Hentzer, M. Givskov, and M. R. Parsek, Mol. Microbiol. **62**, 1264 (2006).
[51] T. Mora and W. Bialek, J Stat Phys **144**, 1 (2011).
[52] W. Bialek, A. Cavagna, I. Giardina, T. Mora, and E. Silvestri, Proc Natl Acad Sci U S A **109**, 4786 (2012).
[53] D. Krotov, J. O. Dubuis, T. Gregor, and W. Bialek, Proc. Natl. Acad. Sci. **111**, 3683 (2014).
[54] C. Furusawa, Phys. Rev. Lett. **208103**, 1 (2012).
[55] M. Nykter, N. D. Price, M. Aldana, S. A. Ramsey, S. A. Kauffman, L. E. Hood, O. Yli-harja, and I. Shmulevich, Proc. Natl. Acad. Sci. **105**, 1897 (2007).
[56] J. M. Beggs and D. Plenz, J. Neurosci. **23**, 11167 (2003).
[57] W. Kong, D. R. Meldgin, J. J. Collins, and T. Lu, Nat. Chem. Biol. **14**, 821 (2018).
[58] H. G. Garcia, H. J. Lee, J. Q. Boedicker, and R. Phillips, Biophys. J. **101**, 535 (2011).

Figures and Figure Captions:

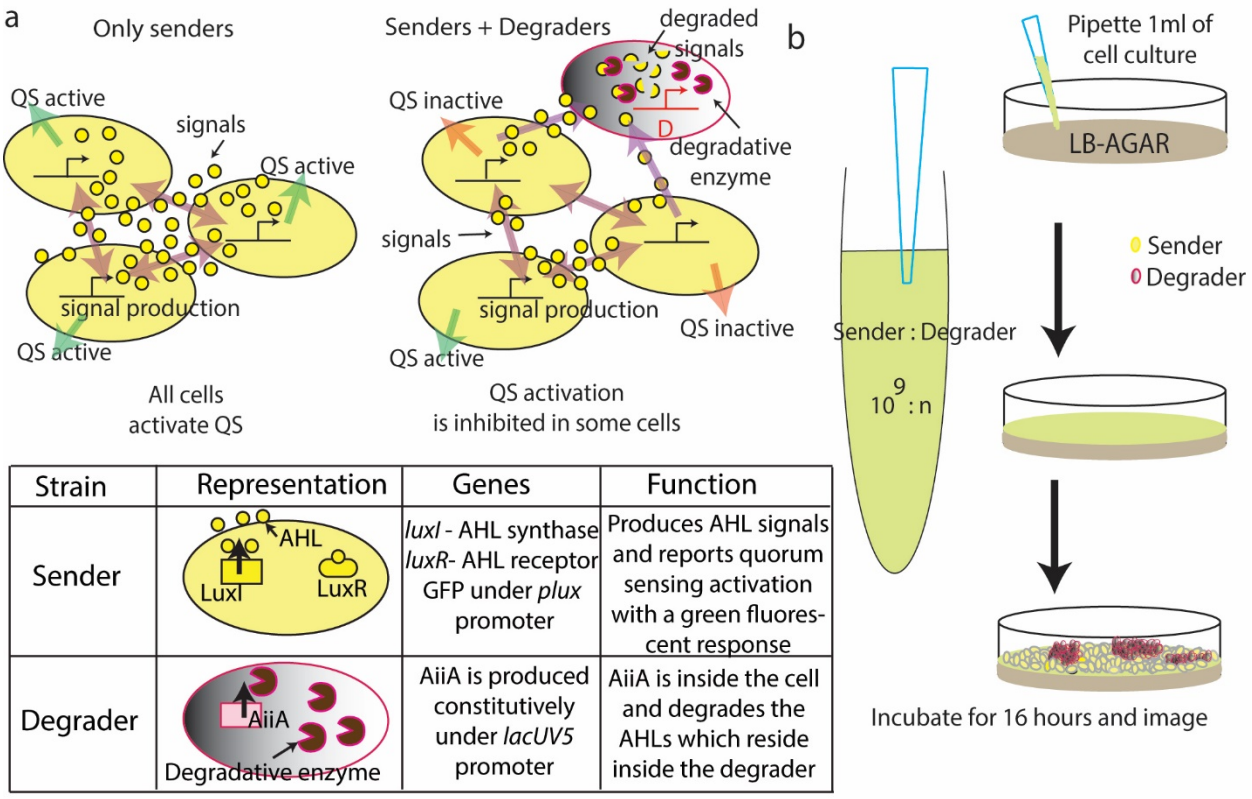

Strain	Representation	Genes	Function
Sender		*luxI* - AHL synthase *luxR*- AHL receptor GFP under *plux* promoter	Produces AHL signals and reports quorum sensing activation with a green fluores-cent response
Degrader		AiiA is produced constitutively under *lacUV5* promoter	AiiA is inside the cell and degrades the AHLs which reside inside the degrader

FIG. 1. Experimental assay to measure spatial patterns of cellular communication in the presence of interference. (a) The sender (yellow) produces an acyl-homoserine lactone (AHL) signal, 3-oxo-C6-HSL, while the degrader (black shaded) produces the AHL degradative enzyme AiiA constitutively. When the senders are in monoculture, quorum sensing is uniformly activated by all cells across the plate. When degraders are introduced, AHLs are degraded resulting in regions where sender cells do not activate quorum sensing. (b) Senders and degraders are mixed at a ratio of 10^9 : n (units of cells), where n varied from 0 to 2 x 10^9 cells. The mixture is loaded into a small petri dish with LB agar.

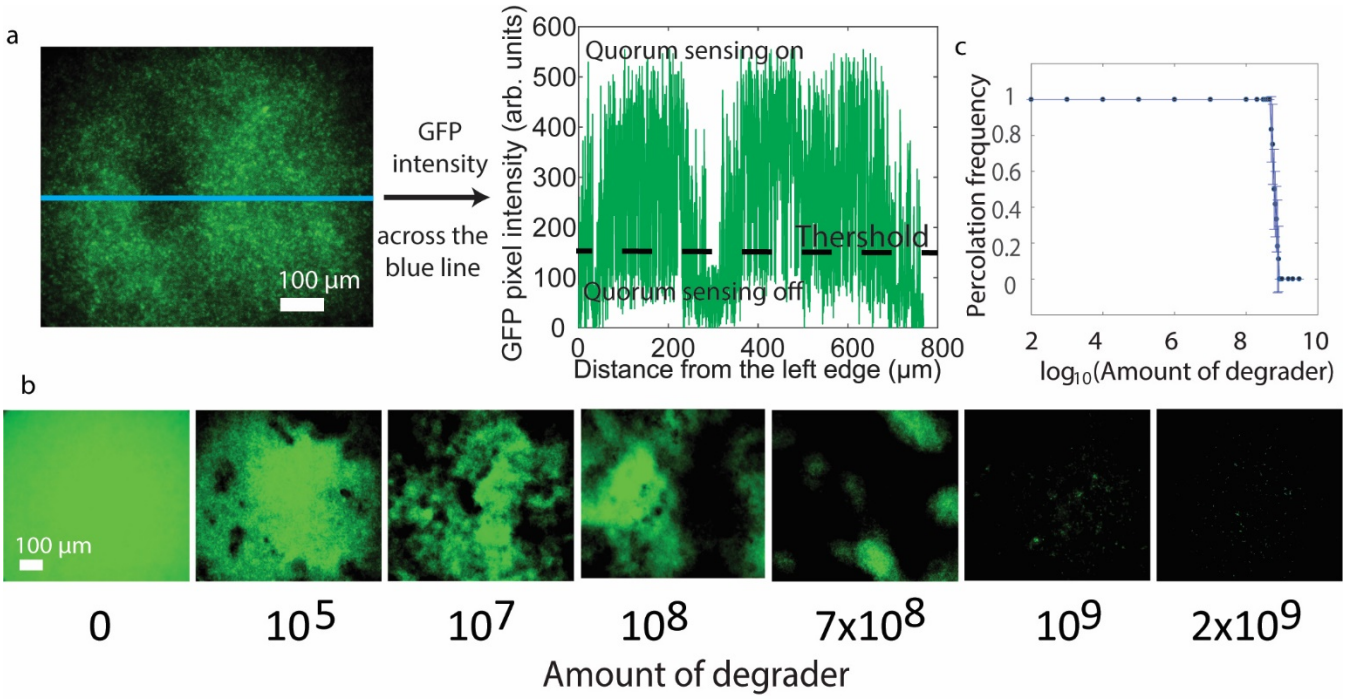

FIG. 2. Experimental demonstration of a degrader-dependent percolation transition. (a) Here we represent the 20x microscopic GFP image, of the sender cells (left) in the presence of degraders at a ratio of 10^9: $6x10^8$ (sender: degrader). The GFP is due to quorum sensing activation. The dark regions in the green fluorescent image is due to the senders not activating quorum sensing due to the presence of degraders, see Fig. S1 [34]. We measured the GFP pixel intensity across the blue line, represented in the fluorescent image, and observed that the fluorescence dips below the threshold value at certain points on the line (see Fig. S2 for further details on the threshold [34]). (b) The 20x fluorescent microscopy images reveal the regions of active (green) and inactive senders (dark) as we increase the amount of degraders. (c) The number of percolation events in our images was measured as a function of the amount of degraders added the plate. Here the data is taken from three replicate plates, with each plate having a minimum of 16 images. The error bars represent the standard error over replicates.

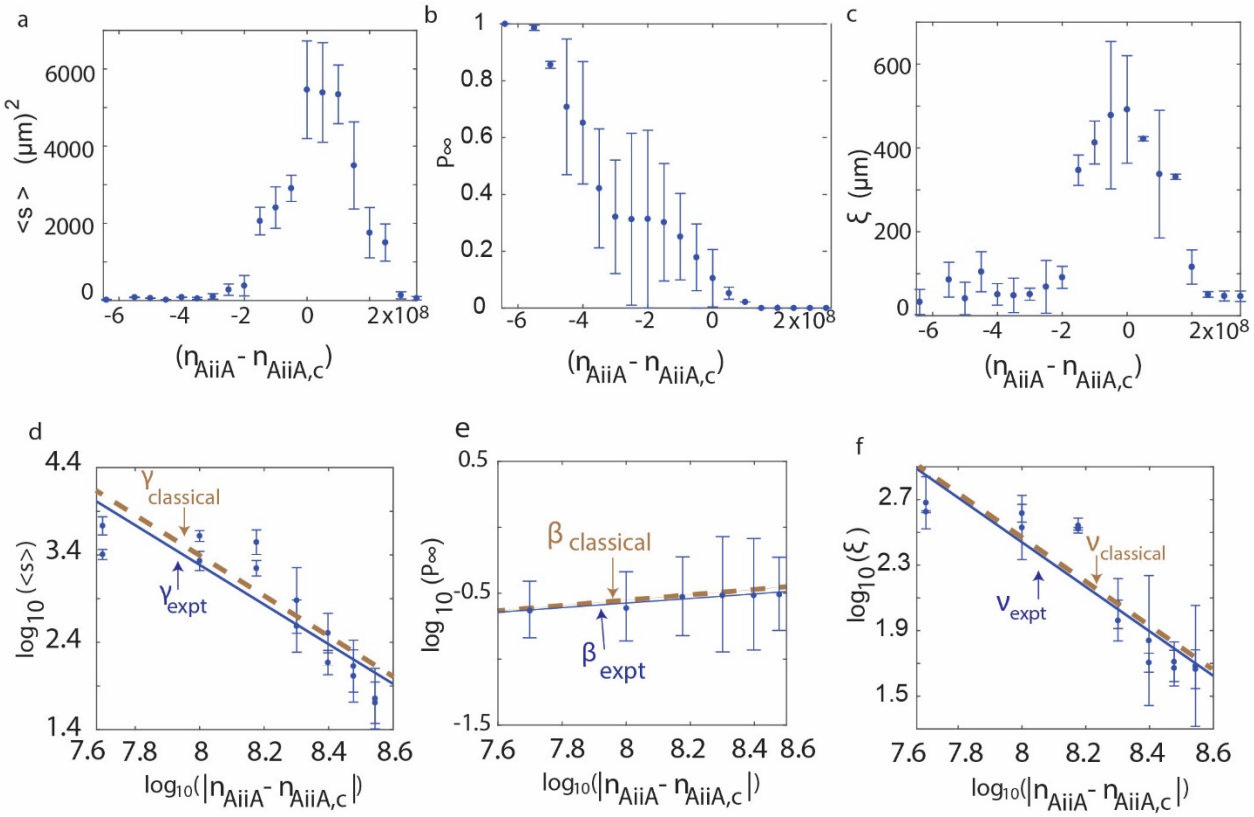

FIG. 3. Scaling quantities from experiments. (a) The average cluster size <s> , (b) the order parameter P_∞ , (c) and the correlation length ξ calculated from experimental data. The error bars represent the standard error from 3 replicate plates and a minimum of 16 images per plate. In (d), (e), (f), we have the $\log_{10}$-$\log_{10}$ transform of the points in the critical region for <s>, P_∞ and ξ respectively, marked as closed blue circles. The slope of the linear fits to these points yields the critical exponents. The blue lines represent the linear fit (least square fit) with the experimentally obtained exponent while the dashed brown lines represent the values from classical percolation theory, listed in Table 1. The error bars in d-f are determined via propagation of the $\log_{10}$ of the uncertainty.

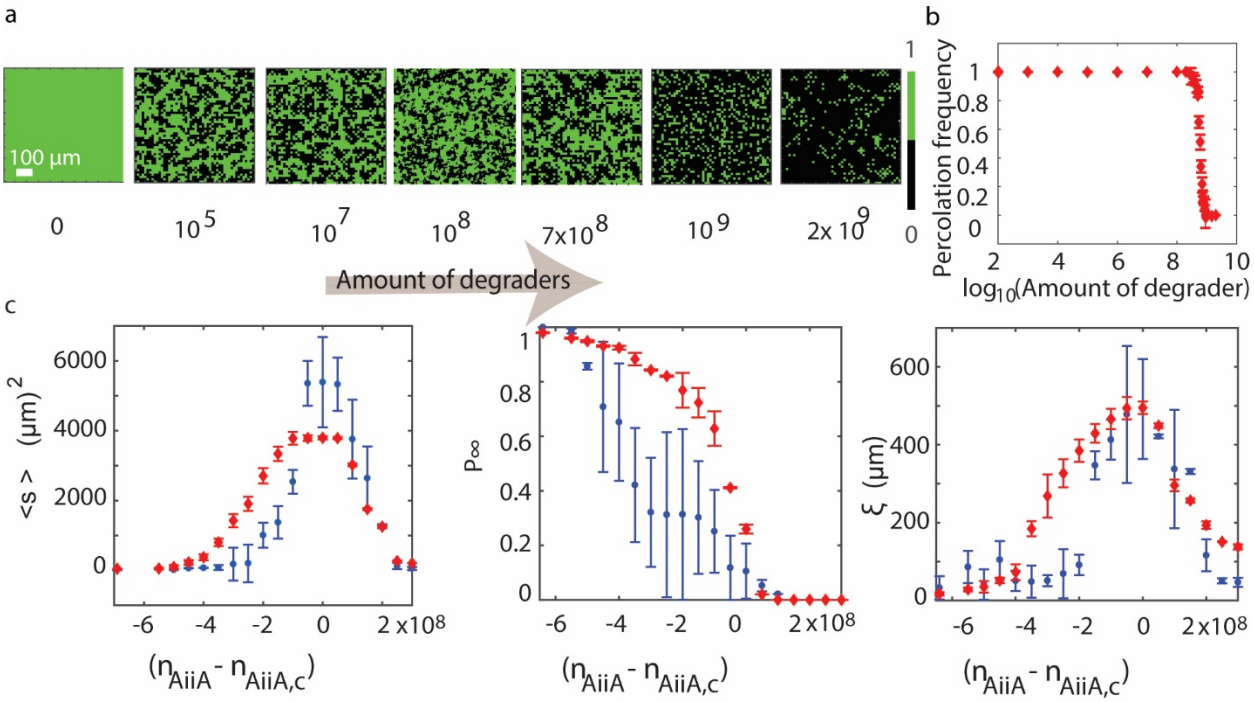

FIG. 4. Simulation of quorum sensing activation in the sender and degrader community. (a) The AHL concentration of the senders from simulations are marked in green, with green indicating signal concentration that exceeded the threshold needed to activate quorum sensing. (b) The frequency of percolation events from the simulations. (c) The average cluster size <s>, the order parameter P_∞ and the correlation length ξ obtained from simulations. The red diamond data points are simulated data while the blue circular data points are experimental data points added for comparison. The error bars for the simulations represent the standard error over 100 repeats.

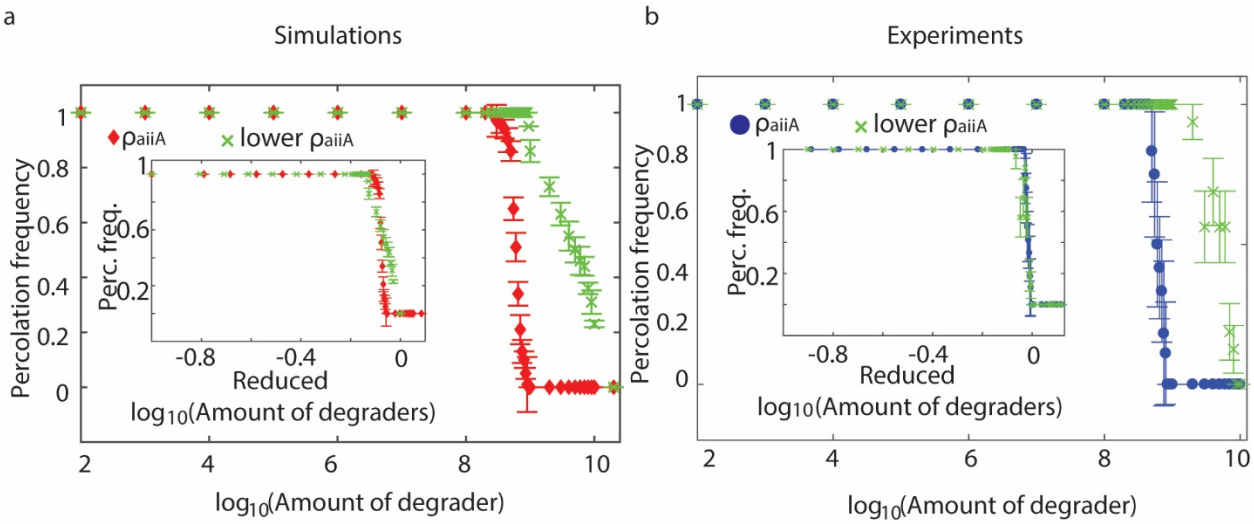

FIG. 5. Changing the production rate of AiiA shifts the critical density. The Percolation frequency (Perc. freq.) (a) from simulations and (b), from experiments for two different production rates(ρ_{aiiA}) of the AiiA enzyme. For both simulations and experiments, the green cross-marked points represent the case when the degraders with lower production rate was used. In simulations, this lower value was $0.6\rho_{aiiA}$. The red diamond data points in simulations represent when the production rate of the degrader enzyme was the original value (ρ_{aiiA}). In experiments, the blue circular data points represent when the normal degrader with production rate ρ_{aiiA} was used. For the degrader with lower production rate, the IPTG level was kept at 1.0 mM such that the production rate of the degradative enzyme was decreased (see Fig. S17 [34]). In the inset we represent the universality in the nature of transition by reducing the x-axis to (log (Amount of degraders) - log (Amount of degraders)$_c$)/ (log (Amount of degraders)$_c$). The error bars for the simulations represent the standard error over 100 iterations. The error bars for the experiments represent the standard error over 3 sets of experiments.